THE JOURNAL OF PHYSICAL CHEMISTRY A

Article

pubs.acs.org/JPCA

# Photodissociation Dynamics of the *i*-Methylvinoxy Radical at 308, 248, and 225 nm Using Fast Beam Photofragment Translational Spectroscopy

Bethan Nichols, Erin. N. Sullivan, Mikhail Ryazanov,† and Daniel M. Neumark*

Department of Chemistry, University of California, Berkeley, California 94720, United States

Chemical Sciences Division, Lawrence Berkeley National Laboratory, Berkeley, California 94720, United States

Supporting Information

**ABSTRACT:** The photodissociation dynamics of the *i*-methylvinoxy ($CH_3COCH_2$) radical have been studied by means of fast beam coincidence translational spectroscopy. The radical was produced by photodetachment of the *i*-methylvinoxide anion at 700 nm, followed by dissociation at 225 nm (5.51 eV), 248 nm (5.00 eV), and 308 nm (4.03 eV). At all three dissociation energies, the major products were found to be $CH_3$ + $CH_2CO$, with a small amount of CO + $C_2H_5$ produced at the higher dissociation energies. Photofragment mass distributions and translational energy distributions were recorded for each wavelength. Comparison of the mass distributions with dissociation of fully deuterated *i*-methylvinoxy aided the assignment of the observed channels. Electronic structure calculations were performed to determine the relative energies of minima and transition states involved in the dissociation and to aid interpretation of the experimental results. The proposed dissociation mechanism involves internal conversion from the initially excited electronic state, followed by dissociation over a barrier on the ground state.

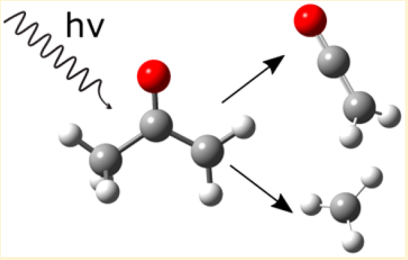


## 1. INTRODUCTION

Substituted vinoxy radicals, such as *i*-methylvinoxy ($CH_3COCH_2$), are important intermediates in combustion reactions between unsaturated hydrocarbons and OH radicals[1] in addition to being the primary products of reactions between O atoms and alkenes.[2] In atmospheric chemistry, *i*-methylvinoxy has been suggested as an intermediate in the reaction between acetone and OH and is of considerable interest due to the abundance of acetone in the troposphere.[3,4] Knowledge of the unimolecular dissociation products and bond dissociation energies of such radical intermediates is necessary to understand the overall complex reaction mechanisms in combustion and atmospheric chemistry. In this work, we employ fast radical beam coincidence translational spectroscopy to gain an understanding of the photochemistry and dynamics of the *i*-methylvinoxy radical.

The spectroscopy and dynamics of the unsubstituted vinoxy radical ($CH_2CHO$) have been the focus of numerous experimental and theoretical studies. Initial interest in the photodissociation dynamics of the vinoxy radical[5] was prompted by the difference between the laser-induced fluorescence (LIF) spectrum,[6,7] which stops abruptly at 30200 $cm^{-1}$, and the UV absorption spectrum,[8] which extends to 35000 $cm^{-1}$. In one of the first studies to examine its photodissociation dynamics, Osborn et al.[5] excited the vinoxy radical to the $\tilde{B}$ excited electronic state and observed two product channels: $CH_3$ + CO and H + $CH_2CO$. The translational energy distributions and branching ratios indicated that dissociation took place on the ground electronic surface following rapid internal conversion from $\tilde{B} \rightarrow \tilde{A} \rightarrow \tilde{X}$ states. Subsequent theoretical work[9] investigated the mechanism for internal conversion, and it was proposed that the $\tilde{B} \rightarrow \tilde{A}$ conversion proceeded via an avoided crossing followed by a radiationless transfer to the ground state via a conical intersection.

In contrast to the wealth of dissociation studies involving the unsubstituted vinoxy radical, far less is known about the photodissociation dynamics of methyl-substituted vinoxy species such as the *i*-methylvinoxy radical. The *i*-methylvinoxy radical has, however, been the focus of a number of other spectroscopic and electronic structure investigations. The UV absorption spectrum has been measured by Cox et al.[10] and more recently by Imrik et al.,[11] showing a strong absorption centered at around 210 nm in addition to a weaker absorption feature at around 315 nm. The latter corresponds to the $\tilde{B}^2A'' \leftarrow \tilde{X}^2A''$ transition, which can be considered to be a $\pi \rightarrow \pi^*$ transition on the carbonyl group.[11,12] It was suggested that the strong absorption centered at around 210 nm could be due to excitation to a higher-lying electronic state. Electronic structure calculations have shown that in the ground electronic state, the radical is predominantly centered on the terminal carbon, as in structure (a) of Figure 1, whereas in the $\tilde{A}^2A'$ and $\tilde{B}^2A''$ excited states, the unpaired electron density is mostly located on the O

**Received:** October 19, 2016
**Revised:** December 16, 2016
**Published:** December 19, 2016





DOI: 10.1021/acs.jpca.6b10570
J. Phys. Chem. A 2017, 121, 579−586

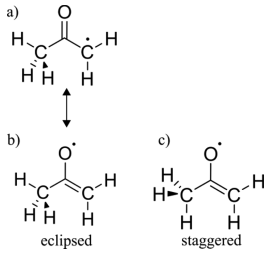


**Figure 1.** Structures of the *i*-methylvinoxy radical.

atom, either in or out of the plane, respectively, similar to the unsubstituted vinoxy radical.[13,14]

LIF studies performed by Williams et al.[12,15] have investigated the $\tilde{X} \rightarrow \tilde{B}$ transition in *i*-methylvinoxy and identified a number of skeletal vibrations in the $\tilde{B}$ state. The LIF spectrum for *i*-methylvinoxy is complicated by the hindered rotation of the methyl group. As illustrated in (b) and (c) of Figure 1, there are two low-energy orientations of the methyl group, labeled staggered and eclipsed. The preferred conformation for the methyl group was determined to be eclipsed for the ground electronic state but staggered in both the $\tilde{A}$ and $\tilde{B}$ excited electronic states,[13,14] as indicated in Figure 1. Similar to the case of unsubstituted vinoxy, an abrupt cutoff in LIF intensity in the *i*-methylvinoxy spectrum was observed at 30000 $cm^{-1}$, which corresponds to an energy of 2700 $cm^{-1}$ above the $\tilde{B}$ state origin.[12] Interestingly, it was found that methyl substitution had very little effect on the onset of the fast radiationless decay process in terms of the total excitation energy; however, in terms of the vibrational energy above the $\tilde{B}$ state origin, the energy difference is much larger. It was suggested that the effect of methyl substitution is to shift the relative energies of two interacting surfaces, thus changing the energy of a surface intersection involved in the rapid internal conversion from the $\tilde{B}$ state to the $\tilde{X}$ state. An alternate suggestion was that the fast decay could indicate the onset of dissociation to the triplet ketene product.[12]

Numerous anion photoelectron spectra have been reported for the *i*-methylvinoxy anion,[13,14,16,17] providing information about the electron affinity of the neutral radical, as well as detailed information on the structure and vibrational frequencies of the anion $\tilde{X}$ state and neutral $\tilde{X}$ and $\tilde{A}$ states. Most recently, Yacovitch et al.[14] used slow electron velocity map imaging (SEVI) to obtain high-resolution photoelectron spectra, through which the hindered rotation of the methyl group in both the anion and neutral *i*-methylvinoxy molecule was observed and characterized. Comparison of experimental photoelectron spectra with hindered rotor and vibrational Franck−Condon simulations demonstrated that there is a change in conformation of the methyl group from staggered in the anion $\tilde{X}^1A'$ state to eclipsed in the neutral $\tilde{X}$ state. This work found the electron affinity for *i*-methylvinoxy to be EA = 1.747 ± 0.002 eV and the $\tilde{A}$ state term energy to be $T_0$ = 1.307 ± 0.002 eV.

In this study, we report results on the photodissociation of the *i*-methylvinoxy radical at 225, 248, and 308 nm. Following the UV excitation of *i*-methylvinoxy, there are a number of thermodynamically accessible channels for dissociation[18−20]

$$CH_3COCH_2 \rightarrow CH_3 + CH_2CO \quad D_0 = 1.21 \text{ eV} \tag{1}$$

$$CH_3COCH_2 \rightarrow C_2H_5 + CO \quad D_0 = 0.56 \text{ eV} \tag{2}$$

$$CH_3COCH_2 \rightarrow C_2H_4 + HCO \quad D_0 = 1.33 \text{ eV} \tag{3}$$

$$CH_3COCH_2 \rightarrow H + CH_2COCH_2 \quad D_0 = 2.77 \text{ eV} \tag{4}$$

$$CH_3COCH_2 \rightarrow OH + C_3H_4 \quad D_0 = 2.80 \text{ eV} \tag{5}$$

We observe photodissociation to channel 1 at all dissociation energies used in this study. At higher wavelengths, some dissociation to channel 2 is observed, but channel 1 remains dominant. We also obtain photofragment mass distributions and translational energy distributions, as well as branching ratios for the two channels that we observe. Our results indicate that following excitation of *i*-methylvinoxy to the $\tilde{B}$ state, there is rapid internal conversion to the $\tilde{X}$ state, followed by dissociation via channel 1 and channel 2 at higher energies. To support our experimental findings, we employ density functional theory (DFT) and Rice−Ramsperger−Kassel−Marcus (RRKM) calculations.

## 2. METHODS

**2.a. Experiment.** The fast beam coincidence translational spectrometer employed in this study has been described in detail previously;[5,21] only the details specific to this work will be discussed here.

The *i*-methylvinoxy anions (*i*-$C_3H_5O^-$) were generated by flowing 80 psi (5.5 bar) of Ar through acetone or, similarly, acetone *d*-6 to produce fully deuterated *i*-$C_3D_5O^-$ ions. The gas mixture was supersonically expanded into the vacuum through an Even−Lavie valve operating at 100 Hz, coupled with a DC grid discharge source[22] to produce *i*-$C_3H_5O^-$ ions. The ions were accelerated to a beam energy of 8 keV and mass-selected using a Bakker type mass spectrometer.[23,24] Mass-selected *i*-$C_3H_5O^-$ ions were subsequently photodetached at 700 nm with a Nd:YAG pumped dye laser (Litron LPY742-100 and Radiant Dyes NarrowScan).

A VMI apparatus was recently installed in the photodetachment region,[25] such that the cloud of detached photoelectrons was extracted perpendicularly to the beam path and velocity-mapped onto a position-sensitive detector consisting of two stacked multichannel plates (MCPs) and a phosphor screen. Events on the screen were then recorded using a video camera and transferred to a computer for analysis. Use of the Abel inversion (BASEX)[26] allows the photoelectron translational energy distributions to be obtained from the recorded images, yielding information on the internal energy of both the ions and neutrals. The velocity mapping field typically results in a slight deflection of the beam of ions; deflector plates at the entrance of the VMI apparatus are used to correct the path of the ions. The photodissociation and photoelectron spectra can be recorded simultaneously, but typically a photoelectron spectrum was recorded briefly prior to performing the photodissociation experiment to verify that the anions produced in the discharge were internally cold.

Following the photodetachment of *i*-$C_3H_5O^-$, any anions remaining in the beam were deflected from the axis using an electric field and the resulting beam of fast, neutral *i*-$C_3H_5O$ radicals passed through a pinhole with 1 mm diameter before being intersected by a UV laser beam, generated by a GAM EX-


DOI: 10.1021/acs.jpca.6b10570
J. Phys. Chem. A 2017, 121, 579−586

50F excimer laser (248 nm, 5.0 eV), a Lambda Physik LPX 300 excimer laser (308 nm, 4.02 eV), or an excimer-pumped dye laser (225 nm, 5.51 eV) (Lambda Physik FL-3002). Photofragments recoiling from the beam axis were detected in coincidence by means of a time-and-position-sensitive Roentdek Hex80 delay-line anode detector[21,27] located 1.4 m from the dissociation region. Any undissociated radicals were blocked by a 2.5 mm radius beam block that sits close to the detector face. For each coincident event, the arrival times and positions of the photofragments were determined and then analyzed to yield the photofragment masses, translational energy distributions, and scattering angles. A given event with a very low or high kinetic energy release will lead to one or both fragments being undetected as a consequence of the finite size of the detector and the presence of the beam block; thus, the detection efficiency varies as a function of translational energy release and scattering angle. To accommodate this limitation, the experimental translational energy distributions presented here have been corrected using a detector acceptor function (DAF).[28]

**2.b. Electronic Structure Calculations.** In order to aid the interpretation of the experimental data, electronic structure calculations were performed using Gaussian 09.[29] DFT was chosen to locate and optimize the structures of the minima and transition states relevant to dissociation via channels 1−3 using the B3LYP density functional and the 6-311++G(3df,2p) basis set. Single-point energy calculations employing the composite G4 method were then performed at the optimized ground-state structures. This method has recently been used for calculation of transition state structures for the dissociation of the vinoxy radical.[30]

## 3. RESULTS

**3.a. Photoelectron Spectrum.** The anion photoelectron spectra for *i*-methylvinoxy and its deuterated analogue have been measured previously,[13,14,16] and the electron affinities were determined to be 1.747 and 1.743 eV, respectively. In our experiment, the photodetachment wavelength (700 nm, 1.771 eV) was selected such that it is only slightly higher in energy than the electron affinity in order to minimize the production of vibrationally hot neutrals. The resulting photoelectron spectrum, shown in Figure 2, looks markedly different from previously published spectra in which the entire Franck−Condon profile was mapped out, with progressions in the neutral $\nu_{14}$ (C−C−C bending) and $\nu_{13}$ (O−C−C bending) mode.[14] A series of peaks are present in the experimental photoelectron spectrum that can be attributed to the lowest-frequency mode, the methyl torsion. In transitioning from the anion $\tilde{X}$ state (staggered) to the neutral $\tilde{X}$ state (eclipsed), there is a large change in methyl group conformation; therefore, a vibrational progression in this mode is expected and has been previously observed.[14] The assignment of the peaks in the photoelectron spectrum is discussed in detail in Section 4a.

**3.b. Photofragment Masses and Translational Distributions.** Photofragment mass and translational energy distributions are determined using the arrival times and positions acquired by the hexanode delay line detector for both photofragments of a given coincident event. The mass ratio of the fragments for a given event is related to their respective displacements from the dissociation center through conservation of momentum. Figure 3 displays photofragment mass distributions for the photodissociation of *i*-methylvinoxy at 308 nm (4.03 eV), 248 nm (5.00 eV), and 225 nm (5.51 eV).

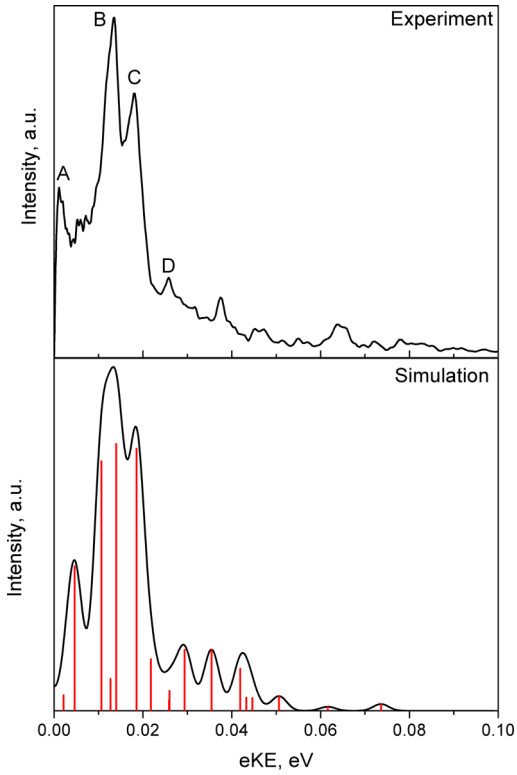


**Figure 2.** Anion photoelectron spectrum of *i*-$C_3H_5O^-$ at $\lambda$ = 700 nm. The top panel displays the experimental PES, while hindered rotor simulations, performed at 200 K, are shown in the bottom panel. A Gaussian convolution of the hindered rotor simulations is also shown, with a Gaussian peak width of $w$ = 0.003 eV.

The dominant channels are clearly centered at around 15 and 42 amu at all three dissociation energies. The longest dissociation wavelength, 308 nm, is the only channel observed in the mass distribution, but as the photon energy is increased, some evidence of a second channel, with product masses of around 28 and 29 amu, can be seen.

Due to the relatively low mass resolution of the photofragment translational spectrometer ($m/\Delta m \approx 10$),[31] it is informative to perform the coincidence measurements with fully deuterated *i*-methylvinoxy. The mass distributions for dissociation of *i*-$C_3H_5O$ and *i*-$C_3D_5O$ at 248 nm are compared in the right panel of Figure 3. The peaks at 15 and 42 in the mass distribution for *i*-$C_3H_5O$ suggest that the dissociation proceeds via channel 1 into $CH_3$ + ketene products. However, it is possible that there could be some contribution from channel 5 as the products OH + $C_3H_4$ are very close in mass to $CH_3$ + ketene. From the right-hand panel of Figure 3, it can be seen that for dissociation of *i*-$C_3D_5O$, the mass distribution peaks at 18 and 44, consistent with dissociation into $CD_3$ and $C_2D_2O$. Although OD and $CD_3$ both have a mass of 18 amu, if there were some contribution to the mass distribution from dissociation via channel 5, we would expect to see the peak at 18 amu to be narrower than the peak at 15 amu as the two peaks will lie on top of one another in the distribution for *i*-$C_3D_5O$, similar to the peak at 44 amu. The minor channel, which appears to peak at approximately 28 and 29 amu for *i*-$C_3H_5O$ could be due to dissociation via either channel 2 or 3. In the mass distribution for *i*-$C_3D_5O$, there is little or no evidence of this channel, making assignment of this channel impossible based on the mass distributions alone. The


DOI: 10.1021/acs.jpca.6b10570
J. Phys. Chem. A 2017, 121, 579−586

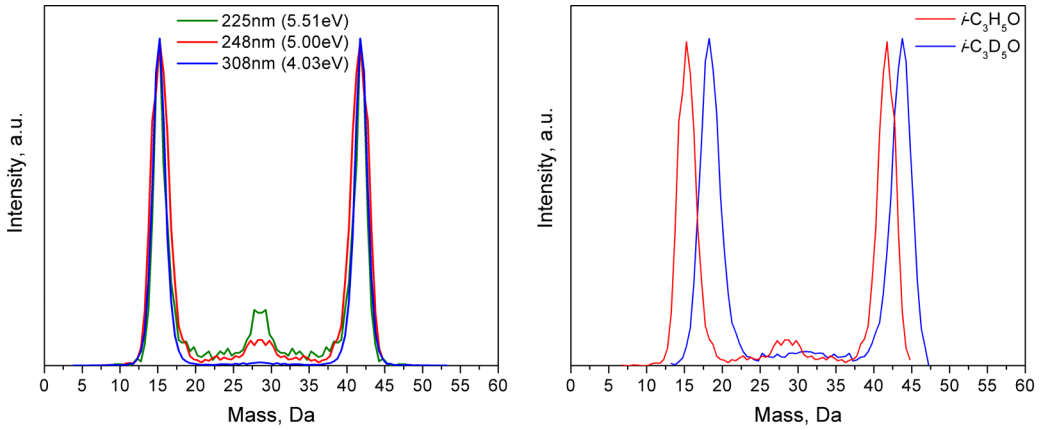


**Figure 3.** (Left) Photofragment mass distributions for $i$-$C_3H_5O$ at dissociation wavelengths of $\lambda$ = 225 (green line), 248 (red line), and 308 nm. (Right) Photofragment mass distributions for $i$-$C_3H_5O$ (red line) and $i$-$C_3D_5O$ (blue line) at a dissociation wavelength of $\lambda$ = 248 nm.

experimental branching ratios for channel 1:channel 2 are 11:1 and 44:1 for dissociation at 225 and 248 nm, respectively. At 308 nm, very little dissociation via channel 2 is seen; therefore, an accurate determination of the branching ratio is not possible, but it is likely to be larger than 100:1.

Photofragment translational energy distributions for dissociation of $i$-$C_3H_5O$ into $CH_3$ and ketene are shown in Figure 4.

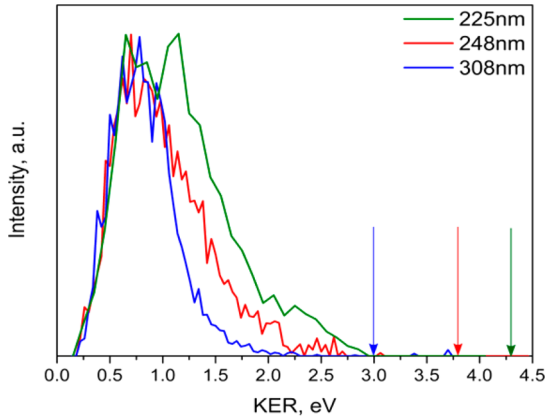


**Figure 4.** Photofragment translational energy distributions for dissociation of $i$-$C_3H_5O$ to $CH_3$ and ketene at 225 (green line), 248 (red line), and 308 nm (blue line).

At all three dissociation energies, the distribution rises to a peak at around 0.7 eV. The distribution broadens and its tail extends to higher energies as the dissociation energy is increased. The number of events in the minor mass channel was too low to reliably determine translational energy distributions for this channel at all wavelengths under investigation.

Assuming that the $i$-methylvinoxy radicals are internally cold prior to excitation, the translational energy available to the dissociation products is given by

$$E_T = E_{photon} - E_{int} - D_0 \quad (6)$$

where $E_{photon} = h\nu$ is the energy of the excitation photon, $E_{int}$ is the internal energies of the outgoing fragments, and $D_0$ is the bond dissociation energy of the given product channel. This results in maximum product translational energies of 2.99, 3.79, and 4.3 eV for dissociation at 308, 248, and 225 nm, respectively. The maximum translational energy for each wavelength is indicated by an arrow in Figure 4. At all three wavelengths, the angular distributions of the photodissociation products were found to be isotropic.

In the dissociation experiment, some background coincident events were detected that were observed even without the UV dissociation laser. After investigation, we concluded that these background events were caused by neutral $i$-$C_3H_5O$ absorbing a second 700 nm photon from the detachment laser. Given that the $\tilde{A}$ state term energy has been previously reported to be 1.037 eV,[14] it is reasonable that the radical is, through the second photon absorption, undergoing excitation to the $\tilde{A}$ state, followed by dissociation via channel 1. After intersection with the 700 nm laser beam, the neutral radicals pass through a 1 mm pinhole before absorbing a UV photon. Therefore, only dissociation events with very small kinetic energies would pass through this pinhole and can largely be rejected during the analysis. However, UV dissociation events with a kinetic energy release of below approximately 0.5 eV may be contaminated by this process.

## 4. DISCUSSION

**4.a. Photoelectron Spectrum.** In order to assign the peaks observed in the photoelectron spectrum, Franck–Condon simulations were performed, employing a 1D hindered rotor model[15,32−34] as in the previous work of Yacovitch et al.[14] The barrier heights used in the hindered rotor simulations were 123 and 890 $cm^{-1}$ for the radical and anion, respectively. As discussed in section 3a, the lowest-energy orientation of the methyl group changes from the staggered to eclipsed geometry upon photodetachment, and therefore, the 1D hindered rotor minima are displaced by 60°. Further details on these simulations and the corresponding hindered rotor potentials are provided in the Supporting Information. The simulations were performed at a temperature of 200 K, similar to anion temperatures previously obtained using this DC discharge source.[25]

The agreement between the hindered rotor simulations and experimental photoelectron kinetic energy distribution is good at low electron kinetic energies (peaks A–D). Table 1 gives assignments for the first four peaks in the experimental spectrum. The energy levels are labeled $m^{final}_{initial}$ according to the convention in ref 14. The assignment for peaks A–C are in agreement with the previous work of Yacovitch et al.[14] Differences between the spectrum presented here and that in ref 14 are due to the lower ion temperature obtained in that work (70 K). At higher electron kinetic energies, the


DOI: 10.1021/acs.jpca.6b10570
J. Phys. Chem. A 2017, 121, 579–586

**Table 1. Peak Positions and Hindered Rotor Transition Assignments**[a]

| peak | energy (eV) | hindered rotor transition |
|---|---|---|
| A | 0.002 | $m_{1e}^{5e}$ |
| B | 0.015 | $m_{0a_1}^{3a_1}/m_{1e}^{4e}$ |
| C | 0.019 | $m_{1e}^{2e}$ |
| D | 0.026 | $m_{2e}^{5e}$ |

[a]The peak labels refer to the labels in Figure 2.

assignment for the experimental peaks is not as clear as the peak heights and positions differ between the experimental and simulated spectra. One possible reason for this is that all peaks above an electron kinetic energy of 0.025 eV are hot bands; discrepancies between experiment and simulation could thus be caused by coupling of the torsional mode with low-frequency vibrations at higher energies, leading to a breakdown in the 1D hindered rotor model.

**4.b. Photodissociation Dynamics of *i*-Methylvinoxy.** The results presented in section 3b indicated that for all three photon energies employed in this study the dominant dissociation products are $CH_3$ and ketene. The dissociation of *i*-methylvinoxy via channel 1 can result in either the singlet or triplet ketene product, depending on the dynamics at the intersection of the relevant potential energy surfaces. At all three dissociation wavelengths employed in this work, the triplet ketene product is energetically accessible, and this pathway has previously been proposed as a possible cause for the sharp decrease in fluorescence lifetime of the $\tilde{B}$ state of *i*-methylvinoxy.[12] However, the experimental translational energy distributions presented in Figure 4 are generally not consistent with dissociation to triplet ketene. For example, the maximum translational energy available to $CH_3$ + triplet ketene for dissociation at 308 nm is 0.4 eV, but the observed translational energy distribution extends to around 2.0 eV and has very little intensity below 0.4 eV.

One aim of the current investigation is to establish whether the photodissociation of *i*-methylvinoxy proceeds along an electronically excited state surface or via decay to the electronic ground state followed by statistical dissociation. To address this issue, we consider the dependence of the translational energy distributions on excitation energy, the overall shape of these distributions, and the product branching between major and minor channels.

As discussed in section 1, the UV absorption spectrum shows a weak absorption feature at around 315 nm and a stronger absorption centered at around 210 nm. The feature at 310 nm corresponds to the $\tilde{B}^2A'' \leftarrow \tilde{X}^2A''$ transition, while it has been suggested that the latter feature could be due to excitation to a higher-energy $\tilde{C}$ state.[11] At 308 nm, only the $\tilde{B}$ state is energetically accessible; however, at 248 and 225 nm, which are in between the two peaks in the UV absorption spectrum, it is possible that there could be some excitation to the $\tilde{C}$ state. Nevertheless, the photofragment translational energy distributions show similar features at all three wavelengths, suggesting that the dynamics at all three dissociation energies are similar.

At all three dissociation energies considered in this work, the translational energy distributions peak at around 0.7 eV, which is much lower than the maximum energetically allowed for each dissociation energy. The combination of a weak dependence of the translational energy distribution peak on photodissociation energy and the peak position occurring above $E_T = 0$, but at much lower energy than the maximum allowed, suggests that the photodissociation could be occurring on the ground state, but with a small exit barrier with respect to the photodissociation products. For such a process, the energy is statistically distributed prior to encountering the barrier on the reaction coordinate, but after the barrier, the energy is released rapidly, resulting in a translational energy distribution that peaks around or below the barrier height.[35] The exit barrier with respect to $CH_3$ + ketene products is 0.66 eV, close to the peak of the photofragment translational distribution.

It is useful to compare the experimental translational energy distributions to the case in which dissociation proceeds along a reaction coordinate that has no exit barrier to the dissociation products. In this scenario, the translational energy distribution can be modeled as a prior distribution, using the equation[36,37]

$$P(E_T \| E_{av}) \propto E_T^{1/2} \cdot \rho_{vr}(E_{av} - E_T) \quad (7)$$

where $E_T$ is the translational energy, $E_{av}$ is the available energy above the dissociation energy, and $\rho_{vr}(E_{av} - E_T)$ is the density of rovibrational states of the dissociation products. For the model presented here, the density of rotational states was assumed to be constant, and the vibrational density of states was calculated using a semiclassical model.[38] The calculated prior distributions are compared with experimental distributions in Figure 5. There are clear differences between the two sets of translational energy distributions, with the prior distribution $P(E_T)$ peaking very close to $E_T = 0$, rather than at around 0.7 eV for the experimental distributions. One explanation for this disparity could be that the condition under which the prior distribution model is valid, that is, statistical dissociation on the ground state with no exit barrier, is not

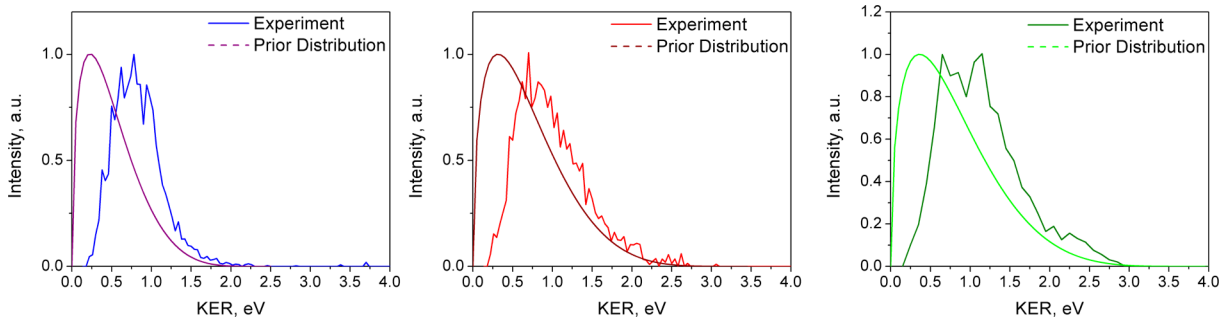


**Figure 5.** Photofragment translational energy distributions for dissociation of *i*-$C_3H_5O$ to $CH_3$ and ketene at 225 (right panel), 248 (middle panel), and 308 nm (left panel). The experimental translational energy distributions are compared with prior distribution calculations that are shown by the dotted line in each panel.



DOI: 10.1021/acs.jpca.6b10570
J. Phys. Chem. A 2017, 121, 579−586

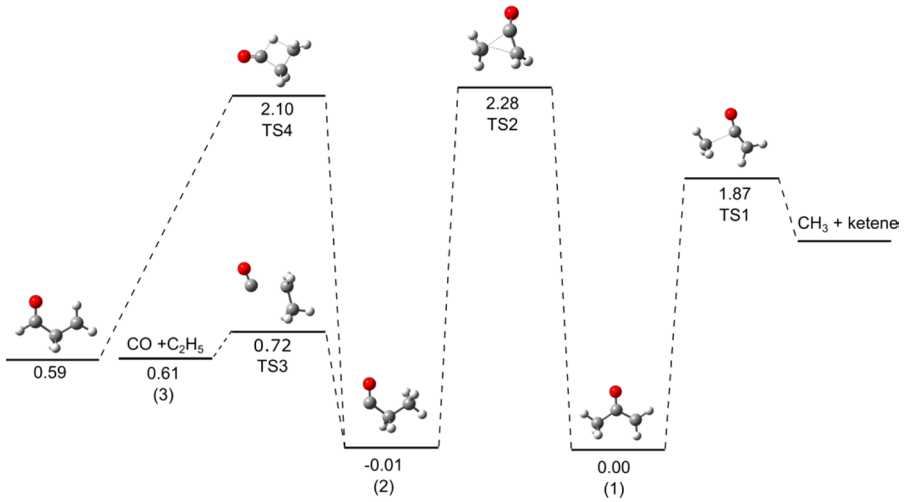


**Figure 6.** Schematic of the calculated potential energy surface involved for *i*-methylvinoxy photodissociation. Energies, given in eV, are relative to the ground state of *i*-methylvinoxy and are calculated at the B3LYP 6-311++G(3df,2p) level of theory for transition state structures and using the G4 composite method for the ground-state structures, other than for TS1. The value for TS1 is from ref 1 and is calculated at the UCCSD(T)-F12b/cc-PVQZ-F12 level of theory.

applicable for *i*-methylvinoxy dissociation to $CH_3$ + ketene. Studies on similar systems that undergo dissociation over a small barrier have found that more energy is partitioned into product translational energy than predicted by the prior distribution.[39,40] This further lends confidence to our suggestion that the dynamics for this channel are consistent with dissociation over a small barrier on the ground state of *i*-methylvinoxy.

From Figure 6, it can be seen that all other possible dissociation channels require an isomerization step over TS2 (2.28 eV) prior to dissociation, which is higher in energy than the barrier to dissociation (TS1, 1.87 eV) to $CH_3$ and ketene products. At 248 and 225 nm, there is evidence of a minor second channel, with product masses of 28 and 29, as shown in Figure 3. Because both channels 2 and 3 have the same product masses, it is not possible to assign this channel on the basis of mass alone. In order to dissociate along channel 2 or 3, the radical must first isomerize to form the propionyl radical via TS2. Dissociation to CO + $C_2H_5$ products (channel 2) can then proceed over a small barrier (TS3, 0.72 eV) directly to the products. On the other hand, to form HCO + $C_2H_4$ (channel 3), an additional isomerization step would have to take place over a much larger barrier (TS4, 2.10 eV) followed by a subsequent dissociation over a barrier. It is therefore likely that after isomerization to the propionyl radical the major dissociation products are CO + $C_2H_5$, and we assign the minor channel to channel 2.

Further information on the mechanism of dissociation for channels 1 and 2 comes from consideration of the product branching ratios of channels 1 and 2. As discussed previously, the barrier along the reaction coordinate for channel 1 is lower in energy than the isomerization barrier for channel 2. TS1 is also likely to be a "looser" transition state than TS2 as it involves the breaking of a bond rather than rearrangement. It is therefore unsurprising that channel 1 is the major channel at all three dissociation wavelengths.

RRKM calculations were performed to model the competing dissociation pathways and compare with the experimental branching ratios. The RRKM rate constant is given by[38]

$$k(E) = \frac{W^{\ddagger}(E - E_0)}{h\rho(E)} \quad (8)$$

where $W^{\ddagger}(E - E_0)$ is the total number of vibrational states at the transition state, which is at energy $E_0$ above the ground state of the reactant, $h$ is Planck's constant, and $\rho(E)$ is the density of vibrational states of the ground-state reactant. Both $W^{\ddagger}(E - E_0)$ and $\rho(E)$ are calculated using the Beyer–Swinehart algorithm[41] and the vibrational frequencies for the ground and transition states from the electronic structure calculations described in section 2b and discussed in the Supporting Information. The $CH_3$ torsional mode is treated as a hindered rotation for ground-state *i*-methylvinoxy and TS1. For dissociation via channel 2, isomerization over TS2 is likely to be the rate-limiting step; therefore, branching ratios can be computed from the rates of passage over TS1 and TS2. RRKM rate constants and branching ratios are compared with experimental branching ratios in Table 2. The RRKM calculations predict that for all wavelengths, channel 1 will be the dominant dissociation channel, in agreement with what we observe experimentally. Additionally, the RRKM calculations predict that as the dissociation energy increases, there will be more of a contribution from dissociation via channel 2 and are in reasonable agreement with the experimental branching ratios. At a dissociation energy of 4.02 eV, the contribution to the experimental signal from channel 2 is so low that it is difficult to accurately determine the branching ratio at this energy.

**Table 2. RRKM Rate Constants ($s^{-1}$) and Branching Ratios for Each Photon Energy (eV) with Corresponding Experimental Branching Ratios**

| photon energy | $k_{\text{channel 1}}$ | $k_{\text{channel 1}}$ | (1)/(2) RRKM | (1)/(2) experimental |
|---|---|---|---|---|
| 5.51 | $3.12 \times 10^{11}$ | $1.35 \times 10^{10}$ | 23:1 | 11:1 |
| 5.00 | $1.68 \times 10^{11}$ | $5.82 \times 10^{9}$ | 29:1 | 44:1 |
| 4.02 | $3.27 \times 10^{10}$ | $6.14 \times 10^{8}$ | 53:1 | >100:1 |

There have been a number of previous studies that have investigated the dissociation of the closely related vinoxy



DOI: 10.1021/acs.jpca.6b10570
J. Phys. Chem. A 2017, 121, 579–586

radical. Osborn et al.[5] observed dissociation to H + ketene and $CH_3$ + CO, analogous to channels 1 and 2, respectively, with a branching ratio of 4:1 following $\tilde{B} \leftarrow \tilde{X}$ excitation. This branching ratio was in good agreement with RRKM calculations, and the mechanism proposed was that dissociation took place on the ground electronic surface following rapid internal conversion from $\tilde{B} \rightarrow \tilde{A} \rightarrow \tilde{X}$ states. Miller et al.[42] studied dissociation of the vinoxy radical produced directly in the $\tilde{X}$ state and observed a branching ratio for the H + ketene channel that was much lower than that predicted by RRKM theory. It was suggested that this disagreement could be due to the presence of a conical intersection at planar geometries; however, a subsequent theoretical investigation concluded that this was unlikely.[43] Most recently, Lam et al.[30] used 157 nm photodissociation of chloroacetaldehyde to prepare the vinoxy radical directly in the $\tilde{A}$ and $\tilde{B}$ states and observed both H + ketene and $CH_3$ + CO products. Although they found that H + ketene was the dominant channel, agreement of the experimental data with RRKM calculations was poor, and therefore, it was proposed that the barrier to H + ketene dissociation should be increased by around 0.1 eV from the G4 calculated value. Although agreement between experiment and RRKM theory appears poor for the dissociation of the vinoxy radical, it has generally been concluded in both experimental[5,30] and theoretical[9] investigations that vinoxy radicals produced in their $\tilde{A}$ or $\tilde{B}$ states undergo internal conversion and subsequent dissociation on the ground electronic state.

The photodissociation dynamics of *i*-methylvinoxy show many similarities to those of vinoxy, with both systems showing rapid internal conversion to the ground electronic state, followed by dissociation over a barrier. For both systems, two dissociation channels can be observed, one involving direct bond cleavage (channel 1) or isomerization followed by dissociation (channel 2). The barrier to bond cleavage is similar for both radicals, 1.83 and 1.87 eV in the vinoxy[30] and *i*-methylvinoxy systems, respectively. In contrast, the barrier to isomerization is much higher for the *i*-methylvinoxy radical (2.28 eV), compared with 1.76 eV for vinoxy isomerization to the acetyl radical ($CH_3CO$). It is therefore unsurprising that the branching ratio for channel 2 is much lower than that for the analogous products in vinoxy dissociation.

## 5. CONCLUSIONS

The current work has studied the photodissociation dynamics of the *i*-methylvinoxy radical at 225, 248, and 308 nm by means of fast beam coincidence translational spectroscopy. The dominant photofragment products at all examined dissociation energies were $CH_3$ + singlet ketene, with a minor channel corresponding to dissociation to CO + $C_2H_5$ appearing at the higher dissociation energies. From the photofragment translational energy distributions, it was concluded that the ketene product is produced in its ground electronic state. The experimentally determined translational energy distributions were found to be consistent with a dissociation mechanism that involves internal conversion from the initially excited electronic state to the ground state, followed by dissociation over a barrier. Experimental product branching ratios were compared with RRKM calculations. The RRKM calculations predicted the dominant channel to be $CH_3$ + ketene with a small contribution from CO + $C_2H_5$, which increases with photon energy, in agreement with experimental observations. Disagreement in the absolute values of the product branching ratios could be due to slight underestimation of TS1 (or overestimation of TS2), as has been suggested for the closely related vinoxy radical.

## ■ ASSOCIATED CONTENT

### Supporting Information

The Supporting Information is available free of charge on the ACS Publications website at DOI: 10.1021/acs.jpca.6b10570.

Further details on the 1D hindered rotor simulations and geometries of structures presented in Figure 6 (PDF)

## ■ AUTHOR INFORMATION


### Corresponding Author

*E-mail: dneumark@berkeley.edu.

### ORCID

Bethan Nichols: 0000-0002-0130-6963

### Present Address

†M.R.: JILA 440 University Ave., Boulder, Colorado 80309, USA.


### Notes

The authors declare no competing financial interest.

## ■ ACKNOWLEDGMENTS

This work was supported by the Director, Office of Science, Office of Basic Energy Sciences, and by the Division of Chemical Sciences, Geosciences, and Biosciences of the U.S. Department of Energy at LBNL under Contract No. DE-AC02-05CH11231.

## ■ REFERENCES


(1) Zádor, J.; Miller, J. A. Adventures on the $C_3H_5O$ Potential Energy Surface: OH+ Propyne, OH+ Allene and Related Reactions. *Proc. Combust. Inst.* **2015**, *35*, 181−188.

(2) Leonori, F.; Balucani, N.; Nevrly, V.; Bergeat, A.; Falcinelli, S.; Vanuzzo, G.; Casavecchia, P.; Cavallotti, C. Experimental and Theoretical Studies on the Dynamics of the O ($^3$P)+ Propene Reaction: Primary Products, Branching Ratios, and Role of Intersystem Crossing. *J. Phys. Chem. C* **2015**, *119*, 14632−14652.

(3) Singh, H. B.; Kanakidou, M.; Crutzen, P.; Jacob, D. High Concentrations and Photochemical Fate of Oxygenated Hydrocarbons in the Global Troposphere. *Nature* **1995**, *378*, 50−54.

(4) Wollenhaupt, M.; Carl, S.; Horowitz, A.; Crowley, J. Rate Coefficients for Reaction of Oh with Acetone between 202 and 395 K. *J. Phys. Chem. A* **2000**, *104*, 2695−2705.

(5) Osborn, D. L.; Choi, H.; Mordaunt, D. H.; Bise, R. T.; Neumark, D. M.; Rohlfing, C. M. Fast Beam Photodissociation Spectroscopy and Dynamics of the Vinoxy Radical. *J. Chem. Phys.* **1997**, *106*, 3049−3066.

(6) Inoue, G.; Akimoto, H. Laser-Induced Fluorescence of the $C_2H_3O$ Radical. *J. Chem. Phys.* **1981**, *74*, 425−433.

(7) DiMauro, L.; Heaven, M.; Miller, T. A. Laser Induced Fluorescence Study of the $\tilde{B}\ ^2A'' \rightarrow \tilde{X}\ ^2A''$ Transition of the Vinoxy Radical in a Supersonic Free Jet Expansion. *J. Chem. Phys.* **1984**, *81*, 2339−2346.

(8) Hunziker, H.; Kneppe, H.; Wendt, H. Photochemical Modulation Spectroscopy of Oxygen Atom Reactions with Olefins. *J. Photochem.* **1981**, *17*, 377−387.

(9) Matsika, S.; Yarkony, D. R. Photodissociation of the Vinoxy Radical through Conical, and Avoided, Intersections. *J. Chem. Phys.* **2002**, *117*, 7198−7206.

(10) Cox, R.; Munk, J.; Nielsen, O. J.; Pagsberg, P.; Ratajczak, E. Ultraviolet Absorption Spectra and Kinetics of Acetonyl and Acetonylperoxy Radicals. *Chem. Phys. Lett.* **1990**, *173*, 206−210.

(11) Imrik, K.; Farkas, E.; Vasvári, G.; Szilágyi, I.; Sarzyński, D.; Dóbé, S.; Bérces, T.; Márta, F. Laser Spectrometry and Kinetics of




DOI: 10.1021/acs.jpca.6b10570
J. Phys. Chem. A 2017, 121, 579−586

Selected Elementary Reactions of the Acetonyl Radical. *Phys. Chem. Chem. Phys.* **2004**, *6*, 3958−3968.
(12) Williams, S.; Zingher, E.; Weisshaar, J. C. $\tilde{B}\leftarrow\tilde{X}$ Vibronic Spectra and $\tilde{B}$-State Fluorescence Lifetimes of Methylvinoxy Isomers. *J. Phys. Chem. A* **1998**, *102*, 2297−2301.
(13) Alconcel, L. S.; Deyerl, H.-J.; Continetti, R. E. Effects of Alkyl Substitution on the Energetics of Enolate Anions and Radicals. *J. Am. Chem. Soc.* **2001**, *123*, 12675−12681.
(14) Yacovitch, T. I.; Garand, E.; Neumark, D. M. Slow Photoelectron Velocity-Map Imaging of the *i*-Methylvinoxide Anion. *J. Phys. Chem. A* **2010**, *114*, 11091−11099.
(15) Williams, S.; Harding, L. B.; Stanton, J. F.; Weisshaar, J. C. Barrier to Methyl Internal Rotation of 1-Methylvinoxy Radical in the $\tilde{X}$ ($^2A''$) and $\tilde{B}$ ($^2A''$) States: Experiment and Theory. *J. Phys. Chem. A* **2000**, *104*, 10131−10138.
(16) Ellison, G.; Engelking, P.; Lineberger, W. Photoelectron Spectroscopy of Alkoxide and Enolate Negative Ions. *J. Phys. Chem.* **1982**, *86*, 4873−4878.
(17) Foster, R. F.; Tumas, W.; Brauman, J. I. Unimolecular Decomposition and Vibrationally Induced Electron Autodetachment of Acetone Enolate Ion. *J. Chem. Phys.* **1983**, *79*, 4644−4646.
(18) Tsang, W. In *Energetics of Organic Free Radicals*; Simões, J. A. M., Greenberg, A., Liebman, J. F., Eds.; Springer, 1996; pp 22−58.
(19) Chase, M. W. *NIST-JANAF Thermochemical Tables*; NIST: Gaithersburg, MD, 1998; pp 1−1951.
(20) Hassouna, M.; Delbos, E.; Devolder, P.; Viskolcz, B.; Fittschen, C. Rate and Equilibrium Constant of the Reaction of 1-Methylvinoxy Radicals with $O_2$: $CH_3COCH_2 + O_2 <-> CH_3COCH_2O_2$. *J. Phys. Chem. A* **2006**, *110*, 6667−6672.
(21) Harrison, A. W.; Lim, J. S.; Ryazanov, M.; Wang, G.; Gao, S.; Neumark, D. M. Photodissociation Dynamics of the Thiophenoxy Radical at 248, 193, and 157 Nm. *J. Phys. Chem. A* **2013**, *117*, 11970−11978.
(22) Garand, E.; Yacovitch, T. I.; Neumark, D. M. Slow Photoelectron Velocity-Map Imaging Spectroscopy of $C_2N^-$, $C_4M^-$, and $C_6N^-$. *J. Chem. Phys.* **2009**, *130*, 064304.
(23) Bakker, J. A Beam-Modulated Time-of-Flight Mass Spectrometer. I. Theoretical Considerations. *J. Phys. E: Sci. Instrum.* **1973**, *6*, 785.
(24) Bakker, J. A Beam-Modulated Time-of-Flight Mass Spectrometer. II. Experimental Work. *J. Phys. E: Sci. Instrum.* **1974**, *7*, 364.
(25) Harrison, A. W.; Ryazanov, M.; Sullivan, E. N.; Neumark, D. M. Photodissociation Dynamics of the Methyl Perthiyl Radical at 248 and 193 Nm Using Fast-Beam Photofragment Translational Spectroscopy. *J. Chem. Phys.* **2016**, *145*, 024305.
(26) Dribinski, V.; Ossadtchi, A.; Mandelshtam, V. A.; Reisler, H. Reconstruction of Abel-Transformable Images: The Gaussian Basis-Set Expansion Abel Transform Method. *Rev. Sci. Instrum.* **2002**, *73*, 2634−2642.
(27) Ryazanov, M.; Harrison, A. W.; Wang, G.; Crider, P. E.; Neumark, D. M. Investigation of 3-Fragment Photodissociation of $O_3$ at 193.4 and 157.6 nm by Coincident Measurements. *J. Chem. Phys.* **2014**, *140*, 234304.
(28) Continetti, R.; Cyr, D.; Osborn, D.; Leahy, D.; Neumark, D. Photodissociation Dynamics of the $N_3$ Radical. *J. Chem. Phys.* **1993**, *99*, 2616−2631.
(29) Frisch, M. J.; Trucks, G. W.; Schlegel, H. B.; Scuseria, G. E.; Robb, M. A.; Cheeseman, J. R.; Scalmani, G.; Barone, V.; Mennucci, B.; Petersson, G. A.; et al. *Gaussian 09*; Gaussian, Inc.: Wallingford, CT, 2009.
(30) Lam, C.-S.; Adams, J. D.; Butler, L. J. The Onset of H + Ketene Products from Vinoxy Radicals Prepared by Photodissociation of Chloroacetaldehyde at 157 nm. *J. Phys. Chem. A* **2016**, *120*, 2521−2536.
(31) Cyr, D.; Leahy, D.; Osborn, D.; Continetti, R.; Neumark, D. Fast Beam Photodissociation of the $CH_2NO_2$ Radical. *J. Chem. Phys.* **1993**, *99*, 8751−8764.
(32) Pitzer, K. S.; Gwinn, W. D. Energy Levels and Thermodynamic Functions for Molecules with Internal Rotation I. Rigid Frame with Attached Tops. *J. Chem. Phys.* **1942**, *10*, 428−440.
(33) Pitzer, K. S. Energy Levels and Thermodynamic Functions for Molecules with Internal Rotation: II. Unsymmetrical Tops Attached to a Rigid Frame. *J. Chem. Phys.* **1946**, *14*, 239−243.
(34) Kilpatrick, J. E.; Pitzer, K. S. Energy Levels and Thermodynamic Functions for Molecules with Internal Rotation. III. Compound Rotation. *J. Chem. Phys.* **1949**, *17*, 1064−1075.
(35) Wodtke, A. M.; Hintsa, E. J.; Lee, Y. T. Infrared Multiphoton Dissociation of Three Nitroalkanes. *J. Phys. Chem.* **1986**, *90*, 3549−3558.
(36) Baer, T.; Hase, W. L. *Unimolecular Reaction Dynamics: Theory and Experiments*; Oxford University Press: New York, 1996.
(37) Leyh, B.; Gridelet, E.; Locht, R.; Lorquet, J.-C. Analysis of Kinetic Energy Release Distributions by the Maximum Entropy Method. *Int. J. Mass Spectrom.* **2006**, *249-250*, 330−339.
(38) Marcus, R.; Rice, O. The Kinetics of the Recombination of Methyl Radicals and Iodine Atoms. *J. Phys. Chem.* **1951**, *55*, 894−908.
(39) Mordaunt, D. H.; Osborn, D. L.; Neumark, D. M. Nonstatistical Unimolecular Dissociation over a Barrier. *J. Chem. Phys.* **1998**, *108*, 2448−2457.
(40) North, S. W.; Blank, D. A.; Gezelter, J. D.; Longfellow, C. A.; Lee, Y. T. Evidence for Stepwise Dissociation Dynamics in Acetone at 248 and 193 nm. *J. Chem. Phys.* **1995**, *102*, 4447−4460.
(41) Beyer, T.; Swinehart, D. Algorithm 448: Number of Multiply-Restricted Partitions. *Commun. ACM* **1973**, *16*, 379.
(42) Miller, J. L.; McCunn, L. R.; Krisch, M. J.; Butler, L. J.; Shu, J. Dissociation of the Ground State Vinoxy Radical and Its Photolytic Precursor Chloroacetaldehyde: Electronic Nonadiabaticity and the Suppression of the H + Ketene Channel. *J. Chem. Phys.* **2004**, *121*, 1830−1838.
(43) Young, R. A.; Yarkony, D. R. A Novel Conical Intersection Topography and Its Consequences: The 1, 2 $^2A$ Conical Intersection Seam of the Vinoxy Radical. *J. Chem. Phys.* **2005**, *123*, 084315−084315.


DOI: 10.1021/acs.jpca.6b10570
*J. Phys. Chem. A* 2017, 121, 579−586